Local estimates of Hölder exponents in turbulent vector fields

Florian Nguyen, Jean-Philippe Laval, Pierre Kestener, Alexey Cheskidov, Roman Shvydkoy, Bérengère Dubrulle

Local estimates of Hölder exponents in turbulent vector fields

F. Nguyen, J-P. Laval
*Univ. Lille, CNRS, ONERA, Arts et Metiers ParisTech, Centrale Lille, FRE 2017-LMFL-Laboratoire de Mécanique des Fluides de Lille-Kampé de Fériet, F-59000, Lille, France**

P. Kestener
Maison de la Simulation CEA, CNRS, Université Paris-Saclay, CEA Saclay, 91190 Gif-sur-Yvette, France

A. Cheskidov and R. Shvydkoy
Department of Mathematics, Statistics, and Computer Science, M/C 249, University of Illinois, Chicago, IL 60607, USA†

B. Dubrulle
SPEC, CEA, CNRS, Université Paris-Saclay, CEA Saclay, 91190 Gif-sur-Yvette, France

It is still not known whether solutions to the Navier-Stokes equation can develop singularities from regular initial conditions. In particular, a classical and unsolved problem is to prove that the velocity field is Hölder continuous with some exponent $h < 1$ (i.e. not necessarily differentiable) at small scales. Different methods have already been proposed to explore the regularity properties of the velocity field, and the estimate of its Hölder exponent h. A first method is to detect of potential singularities via extrema of an "inertial" dissipation $D* = \lim_{\ell\to 0} D_\ell^I$ that is independent on viscosity [1]. Another possibility is to use the concept of multifractal analysis that provides fractal dimensions of the subspace of exponents h. However, the multifractal analysis is a *global statistical* method that only provides a *global* information about local Hölder exponents, via their probability of occurrence. In order to explore the local regularity properties of a velocity field, we have developed a *local statistical* analysis, that estimates locally the Hölder continuity. We have compared outcomes of our analysis, with results using the inertial energy dissipation D_ℓ^I. We observe that the dissipation term indeed gets bigger for velocity fields that are less regular according to our estimates. The exact spatial distribution of the local Hölder exponents however shows non trivial behavior and does not exactly match the distribution of the inertial dissipation.

I. INTRODUCTION.

Viscous incompressible fluids are described by the Incompressible Navier-Stokes equations (INSE) in space-time

$$\begin{aligned} \partial_t u_i + u_j \partial_j u_i &= -\frac{1}{\rho}\partial_i p + \nu \partial_j \partial_j u_i + f_i, \qquad (1)\\ \partial_j u_j &= 0, \end{aligned}$$

where Einstein summation convention over repeated indices is used and $u_i(x,y,z,t)$ is the velocity field, $p(x,y,z,t)$ the pressure field, ρ the (constant) mass density, $f_i(x,y,z,t)$ some forcing and ν the molecular viscosity. A natural control parameter for the INSE is the Reynolds number $Re = LU/\nu$, which is built using a characteristic length L and velocity U.

Mathematically, it is not known whether a solution of the INSE which is smooth at some initial time remains smooth at all later times. This problem was first addressed by Leray [2] who introduced the notion of weak solutions (i.e. in the sense of distribution). This notion has since remained a framework to explore regularity condition for both INSE and its inviscid limit, the Euler equation. It prompted people to consider weaker regularity conditions on $\boldsymbol{u}$. In particular, a classical and unsolved problem is to prove that the velocity field is Hölder continuous with some exponent $h < 1$ (i.e. not necessarily differentiable) at small scales, i.e. to find under which conditions the following holds:

$$|\boldsymbol{u}(\mathbf{x}+\boldsymbol{\ell}) - \boldsymbol{u}(\mathbf{x})| < C\ell^h. \qquad (2)$$

Let us note that Hölder continuity defined in equation (2) is a weaker regularity condition than differentiability and uses the velocity increment $\delta\mathbf{u}(\mathbf{x},\boldsymbol{\ell}) = \mathbf{u}(\mathbf{x}+\boldsymbol{\ell}) - \mathbf{u}(\mathbf{x})$ as a building block.

A perhaps more tractable problem is to consider local scaling (Hölder) exponents of the velocity fields. They are defined as:

$$h(\boldsymbol{x}) = \lim_{\ell\to 0} \frac{\ln\left(\max_{|\boldsymbol{\ell}|=\ell} |\delta\boldsymbol{u}(\boldsymbol{x},\boldsymbol{\ell})|\right)}{\ln(\ell/L)}, \qquad (3)$$

where L is a characteristic integral length of scale. Mathematically, these exponents are only defined under the assumption that the limit $\nu \to 0$ is taken, before the limit $\ell \to 0$. In the sequel, we consider extension of this definition by intermediate asymptotic in a range of scale

* florian.nguyen@univ-lille.fr
† shvydkoy@uic.edu; acheskid@uic.edu

$\eta_{h(x)} \ll \ell \ll L$, where $\eta_{h(x)} \sim LRe^{-1/(1+h(x))}$. It is however still difficult to estimate directly such local Hölder exponents via a simple fit on velocity increments based on equation (3). Indeed, since accessible resolutions numerically or experimentally do not allow to probe the velocity field at arbitrarily small scale, the range of scales over which the fit is performed is limited. This induces a lot of noise in the determination of $h(x)$, that makes it unreliable.

A *global* statistical method, was developed by Parisi and Frisch [3] to quantify the probability of observation of a singularity of scaling exponent h via a function $C(h)$. From $C(h)$ we may infer the multifractal spectrum as $D(h) = D - C(h)$, where D is the space dimension. The team of A. Arneodo developed a powerful method based on wavelet transform to measure such spectrum for 1D turbulent velocity fields. This method has been applied to experimental measurements of one velocity component at a single point at high Reynolds numbers in [4], where it was shown that the data are compatible with the multifractal picture, with a most probable h close to 1/3. Later Kestener and Arneodo [5] extended the method to 3D signals (3 components of the velocity field), and showed on a numerical simulation that the picture provided by the 1D measurements was still valid, with the most probable h shifting closer to 1/3.

Since the original MFR method is based on statistical properties, it is robust with respect to noise and limited statistics. However, it only provides a *global* information about local Hölder exponents, via their probability of occurrence. In order to explore the regularity properties of a velocity field, it would however be useful to devise a *local statistical* analysis, that keeps the robustness of the global MFR method and quantify *locally* the Hölder continuity, while avoiding pitfalls induced by a naive direct fit of equation (3). In the present paper, we extend recent mathematical results of [6] to multifractal settings to provide the best local estimate of Hölder regularity compatible with the global MFR analysis. Our method is in spirit similar to an inference algorithm based on information theory: the local estimate depends on non-dimensional constants that are are statistically fitted on the available data set. Therefore, the estimate depends on the data set, and can only provide information a posteriori. The larger the data set, the more information available, the better the estimate. In our case, the larger the data set, the lowest values of h can be explored.

The paper is organized as follows: in Section II, we describe the wavelet based velocity increments and our method for anisotropic multifactal analysis. In Section III, we generalize the notion of active volume introduced by [6] and show how it can be used to build a local estimate of the Hölder exponents . The method is tested using a fractional brownian motion in Section IV. It is further implemented on 3D turbulent velocity fields computed using DNS in Section V. Our results are discussed in Section VI.

II. VELOCITY INCREMENTS AND MULTIFRACTAL

Our method relies heavily on velocity increments and multifractal theory. We therefore provide some generalities about velocity increments in appendix A. We then proceed by defining our new approach using wavelet transforms.

A. Wavelet velocity increments

For an incompressible velocity field, both side of the first equation in (A6) are reduced to zero, so we cannot use it to get any information on ϕ, the potential part of the velocity field. The usual velocity increments defined in equation (A2) can be seen as the wavelet transform of the velocity with a Haar wavelet. This motivates us to define wavelet velocity increments $\delta W(\mathbf{u})$ through the smoothed velocity gradient G^ℓ_{ij} and its symmetric and antisymmetric parts defined as:

$$\begin{aligned} G^\ell_{ij} &= \ell \int \frac{d\mathbf{y}}{\ell^3} \nabla_j \Psi\left(\frac{\mathbf{y}}{\ell}\right) u_i(\mathbf{y}), \\ S^\ell_{ij} &= \frac{1}{2}\left(G^\ell_{ij} + G^\ell_{ji}\right), \\ A^\ell_{ij} &= \frac{1}{2}\left(G^\ell_{ij} - G^\ell_{ji}\right), \end{aligned} \tag{4}$$

where $\Psi(\mathbf{x}) = \exp(-x^2/2)/N$ is the Gaussian function. By construction, A^ℓ_{ij} is a function only of the rotational part $\mathbf{Q}$, and S^ℓ_{ii} is a function only of ϕ.

We then define normal, longitudinal and transverse wavelet velocity increments as:

$$\begin{aligned} \delta_L W_\ell(\mathbf{u}) &= \max_{ij} |S^\ell_{ij}|, \\ \delta_P W_\ell(\mathbf{u}) &= \max_{ij} |A^\ell_{ij}|, \\ \delta_G W_\ell(\mathbf{u}) &= \left(\delta_L W_\ell(\mathbf{u})^2 + \delta_P W_\ell(\mathbf{u}^2)\right)^{1/2}. \end{aligned} \tag{5}$$

By construction, $\delta_P W_\ell(\mathbf{u})$ provides information only on the rotational part of the velocity field, while all information regarding the potential part is stored in $\delta_L W_\ell(\mathbf{u})$. The component $\delta_G W_\ell(\mathbf{u})$ gives general scaling properties about the velocity field.

This definition bears some similarity with the definition by Kestener and Arneodo [5], that uses principal values of $|G^\ell_{ij}|$. Like theirs, our definition involves no derivative over velocity fields, so it does not introduce additional noise. However, our definition does not involve computation of singular values, that may generate some noise. So, our definition is the smoothest possible one can imagine that enables to quantify scaling properties of potential and rotational part of a given velocity field.

B. Multifractal theory

The multifractal (hereafter MFR) theory that assumes that the Hölder exponent at scale ℓ, defined as

$$h\left(\boldsymbol{x},\ell\right)=\frac{\ln\left(\max_{|\boldsymbol{\ell}|=\ell}\left|\delta\boldsymbol{u}\left(\boldsymbol{x},\boldsymbol{\ell}\right)\right|\right)}{\ln\left(\ell/L\right)}, \tag{6}$$

follows a large deviation property [3]

$$\text{Prob}\left(h\left(\boldsymbol{x},\ell\right)=h\right)\sim\left(\frac{\ell}{L}\right)^{C(h)}. \tag{7}$$

Formally, $C(h)$ corresponds to the codimension of the set where the local Hölder exponent at scale ℓ is equal to h. From $C(h)$ we may infer the MFR spectrum as $D(h)=D-C(h)$, where D is the space dimension.

1. Computation of the multifractal spectrum

Parisi and Frisch devised in 1987 the first global determination of the multifractal spectrum through the structure functions [3]. The latter are defined from the velocity increments and are supposed to scale as:

$$\langle|\delta u|^p\rangle\propto\ell^{\zeta(p)}. \tag{8}$$

The set of scaling exponents $\zeta(p)$ is then connected to the multifractal spectrum through a Legendre transform:

$$\zeta(p)=min_h(ph+D-D(h)), \tag{9}$$

Assuming the spectrum $D(h)$ is strictly concave, we can apply a variational formula to recover:

$$h(p)=\frac{d\zeta(p)}{dp}. \tag{10}$$

Notice that for $p=0$, $h(0)$ represents the most probable scaling exponent (with $D(h)$ equals to the full space dimension). When $p\to-\infty$, the right part of the MFR spectrum (the more and more regular points) is explored; while when $p\to+\infty$, it is the left part of the MFR spectrum (the more and more singular points). This method is global in the sense that it uses global averages of velocity increments to get the multifractal spectrum, and the set of available Hölder exponents. It provides the probability to observe a given Hölder exponent, but provides no information about their exact location. Other methods have been designed based on structure functions. One notable example is the work of Jensen [7] which uses an inverted version of equation (8) to obtain potentially more accurate results for $p<0$. As we are more interested in probing the less regular region of the velocity field, corresponding to $p>0$, we will not use this method in the following.

2. WTMM method

In 1991, A. Arneodo and his group showed that a much more efficient algorithm of computation of the multifractal spectrum for scalar fields was possible, provided one uses structure functions based on wavelet increments instead of velocity increments. An extension of this method to 3D vector field was developed later by Kestener [5, 8] based on singular value decomposition of the wavelet transform of the velocity gradient $G_{ij}=\partial_j u_i$. Here, we apply their algorithm, using the smooth velocity increments equation (5). The algorithm follows the (*Wavelet Transform Modulus Maxima*) (WTMM) method. We first compute the wavelet transform skeleton, which provides us with a set of lines $\{\mathcal{L}_k\}$ where $\mathcal{L}_k(\ell)$ gives the position of the line indexed by k at scale ℓ. Then, one computes the partition functions for the different type of wavelet based increments as follow:

$$\mathcal{Z}_T(q,\ell)=\sum_{\mathcal{L}_k\in\mathcal{L}(\ell)}\Big(\delta_T W_\ell(\boldsymbol{u})(\mathcal{L}_k(\ell))\Big)^q \tag{11}$$

where T stands for G,L or P, $q\in\mathbb{R}$ and $\mathcal{L}(\ell)$ is the set of lines that exists at scale ℓ.

Those partitions functions behave as a power law of the scale:

$$\mathcal{Z}_T(q,\ell)\propto\ell^{\tau_T(q)}. \tag{12}$$

Then by Legendre transforming $\tau_T(q)$, we get the singularity spectrum $D_T(h)=\min_q(qh-\tau_T(q))$. Alternatively, we can bypass the Legendre transform by computing:

$$h_T(q,\ell)=\sum_{\mathcal{L}_k\in\mathcal{L}(\ell)}\ln|\delta_T W_\ell(\boldsymbol{u})(\mathcal{L}_k(\ell))|\mathcal{W}(q,\mathcal{L}_k,\ell), \tag{13}$$

$$D_T(q,\ell)=\sum_{\mathcal{L}_k\in\mathcal{L}(\ell)}\delta_T W_\ell(\boldsymbol{u})(\mathcal{L}_k(\ell))\ln\Big(\mathcal{W}(q,\mathcal{L}_k,\ell)\Big) \tag{14}$$

where $\mathcal{W}(q,\mathcal{L}_k,\ell)=\frac{1}{\mathcal{Z}_T(q,\ell)}\Big(\delta_T W(\boldsymbol{u},\ell)(\mathcal{L}_k(\ell))\Big)^q$ is a Boltzmann weight computed from the wavelet transform skeleton. These quantities behave as power laws as follows:

$$h_T(q,\ell)\propto\ell^{h_T(q)}, \tag{15}$$

$$D_T(q,\ell)\propto\ell^{D_T(q)} \tag{16}$$

and thus we can recover the singularity spectrum $D_T(h)$.

III. LOCAL CHARACTERIZATION OF MULTIFRACTAL VECTOR FIELDS

The previous section describes a procedure to compute globally a multifractal spectrum. We now describe a method that gives access to estimates of local scaling properties of the velocity field, using the notion of nested active volume described in appendix B.

A. Active volumes and multifractal

We first define $\mathcal{S}_{p,dp}$ as:

$$\mathcal{S}_{p,dp}(\ell) = \left(\frac{\langle (\delta W_\ell(\mathbf{u}))^{p+dp} \rangle}{\langle (\delta W_\ell(\mathbf{u}))^{p} \rangle}, \right)^{1/dp}. \tag{17}$$

The limit as $dp \to 0$ can be computed as:

$$\mathcal{S}_p(\ell) \equiv \mathcal{S}_{p,0}(\ell) = \exp\left(\frac{\langle \ln\left(\delta W_\ell(\mathbf{u})\right) \left(\delta W_\ell(\mathbf{u})\right)^p \rangle}{\langle \left(\delta W_\ell(\mathbf{u})\right)^p \rangle}, \right). \tag{18}$$

One can prove that if $\mathbf{u}$ is multifractal, then :

$$\ln \mathcal{S}_p(\ell) \approx h(p) \ln \ell, \tag{19}$$

which gives access to the value $h(p)$.

We can then define the active volume A_p by:

$$\mathbf{x} \in A_p \quad iff \quad \delta W_\ell(\mathbf{u})(\mathbf{x}) \geqslant c_p \mathcal{S}_p(\ell), \tag{20}$$

where c_p is a scale independent constant, to be fitted consistently later. The property verified by the points in the volume $F_{h(p)}$ is analogous to the property of equation (2). This analogy leads us to define a local singularity exponent $\tilde{h}$ such that all elements $\mathbf{x}$ in A_p verify $\tilde{h}(\mathbf{x}) \leqslant h(p)$. As a result, the frontier of this volume, i.e. the isosurface of the increment $\delta W_\ell(\mathbf{u})$ at value $c_p \mathcal{S}_{p,0}(\ell)$, is identified as the set of the points where the local singularity exponent is $\tilde{h}$.

While the local Hölder exponent h cannot be continuous in the multifractal formalism, the exponent $\tilde{h}$ is continuous by definition. As a result, it is not a real measure of the Hölder exponent. However, it will still be relevant as a measure of the local regularity of the field, hence the name "singularity exponent". This property will be shown by comparing it to other used criteria in the following part.

B. Statistical fitting of the constants

To completely define the field $\tilde{h}(\mathbf{x})$, we need to fix the scale independent constants c_p. These constants are the core of the method, as we can tune them such that the field of singularity exponents $\tilde{h}$ provide a meaningful estimation of the real Hölder exponent smoothed at the scale ℓ. In order to guarantee that the singularity exponent is physically consistent with the global multifractal properties, we set c_p such that the fractal dimensions of the isosurfaces of $\tilde{h}$ match with the multifractal spectrum. More formally:

$$\mathrm{Dim}\left(\left\{ \mathbf{x} | \tilde{h}(\mathbf{x}) = h \right\} \right) = D(h). \tag{21}$$

This leads directly to:

$$\mathrm{Dim}\left(\{ \mathbf{x} | \delta W_\ell(\mathbf{u})(\mathbf{x}) = c_p \mathcal{S}_p(\ell) \} \right) = D(h(p)). \tag{22}$$

In practice the dimension of the isosurfaces of $\tilde{h}$, which are also isosurfaces of the velocity increment, can be measured using a box-counting method. If we note $D^\ell_{bc}(\mathcal{T})$ the box-counting dimension of the isosurface of the velocity increment at scale ℓ of value $\mathcal{T}$, the problem reduces to the following equation:

$$D^\ell_{bc}(c_p \mathcal{S}_p(\ell)) = D(h(p)). \tag{23}$$

The multifractal spectrum are obtained by WTMM, the $\mathcal{S}_p(\ell)$ can be computed from the fields, as well as the function D^ℓ_{bc}. The quantity $h(p)$ can be accessed using the WTMM or power laws on the $S_p(\ell)$ as described in equation (19). As the two methods are expected to give similar results, we will choose in practice the method of fitting power laws over the functions $S_p(\ell)$ for simplicity. The functions involved are not monotonous so equation (23) could have multiple c_p solution. However, we can expect the function $D^\ell_{bc}(\mathcal{T})$ to be concave with a maximum at $\mathcal{T}_{max}$. If we impose $c_p \mathcal{S}_p(\ell) < \mathcal{T}_{max}$ for $p > 0$ and $\mathcal{T}_{max}$ and $c_p \mathcal{S}_p(\ell) > \mathcal{T}_{max}$ for $p < 0$, we get a unique definition of c_p.

Note that our method ensures that the field $\tilde{h}(\mathbf{x})$ can be recovered without computing explicitly the constant c_p. Indeed, we can derive a relationship $\tilde{h}(\mathcal{T})$ from the following equation:

$$D^\ell_{bc}(\mathcal{T}) = D(\tilde{h}), \tag{24}$$

which is derived from equation (21). We can ensure that this function is well defined by imposing $\tilde{h}(\mathcal{T}) < h(p = 0)$ for $\mathcal{T} > \mathcal{T}_{max}$ and reciprocally. While this is the method we will use preferentially to compute maps of $\tilde{h}$, the knowledge of c_p is still pertinent as it is scale independent. This property makes it possible to test the soundness of the method by checking that the procedure, repeated at a different scale, verify the equation (22) for the same value of c_p. Once a value of c_p is computed using one scale, one can then obtain maps of $\tilde{h}$ at any scale in the inertial range for a much lower computational cost. The accuracy of this statements will be discussed in the following.

IV. APPLICATION TO FRACTIONAL BROWNIAN MOTION (FBM)

A. Definition and implementation of fBm

In order to test our analysis, we used synthetic field with well determined fractal behavior. The simplest possible field in this case is the fractional Brownian motion (or fBm), which was already used in [5]. The fBm has properties of isotropy that can be characterized by a single Hölder exponent H for any point.

As a consequence, the multifractal spectrum of a fBm of exponent H in dimension d reduces to a single point:

$$\begin{aligned} D(h) &= d && if \quad h = H, \\ &= -\infty && otherwise. \end{aligned} \tag{25}$$

In this case, the exponent $\tau(q)$ of both the original WTMM method and our variation should have the following expression:

$$\tau(q) = qH - d. \tag{26}$$

The fBm used in the following are generated by filtering the Fourier transform of a white noise. This method gives a good approximation of the expected invariance properties. For all purposes requiring a range of Hölder exponents, it is assumed that this practical realization with a finite number of snapshots of finite size has a wider multifractal spectrum, centered around the theoretical value H. We chose the value of $H = 1/3$ for a 2 dimensions, 3 components (2D3C) fBm. The objective in the following is to recover this value H using both the original WTMM and our variation of it.

B. Test of the global MFR analysis

As a first test and benchmark of our methods, we generate a hundred 2D3C fBm ($H = 1/3$) in squares of size unity with a definition of 4096×4096. The Figure 1 shows the $\tau(q)$ corresponding to the different components, as well as the output of the original WTMM method.

The results of our new method are consistent with the theoretical predictions, although a little less accurate than the native method. The consequence of this lack of accuracy is an estimation of the Hölder exponent $h \approx 0.31$ using the global term, which is slightly inferior to the value of $h \approx 0.33$ evaluated by the original WTMM method. Furthermore, the computation of the perpendicular component suffers from the lack of the third dimension in the provided fields, hence a spectrum spreading over a much wider range of h than expected.

C. Test of the local estimate

In parallel, we can apply our second method to extract the local coefficients $\tilde{h}$ in one field of the same set of fBm. The computation requires to chose a value of ℓ. In the sequel, we fix the value $\ell = 2.8 \times 10^{-3}$ for any computation on the fBm at definite ℓ. This value, corresponding to 11.4 grid points at the resolution of the field, is small enough to probe the small structures and large enough so that wavelets are well resolved. The Figure 2 shows the function $D^{\ell}_{bc}(\mathcal{T})$ resulting from the boxcounting, while the Figure 3 illustrates the power law behavior of $\mathcal{S}_p(\ell)$. The values of h are convincingly independent with respect to p, with very little fluctuations. The value of h obtained is around $h \approx 0.34$, which is slightly higher than the expected value of $H = 1/3$ but still within acceptable range.

Applying the method described to compute fields of $\tilde{h}$ would normally require to match the box-counting dimensions from Figure 2 with the multifractal spectrum from Figure 1. Unfortunately, the degenerated spectrum makes it impractical. A solution is to use the fact that we are working with a monofractal and ensure that for all p, $c_p \mathcal{S}_p(\ell) = \mathcal{T}_{max}$. Considering the fact that it is very difficult to get measurements of box counting dimension that reach 2, the dimension of the space, we also take the liberty to renormalize $D^{\ell}_{bc}(\mathcal{T})$ such that $D^{\ell}_{bc}(\mathcal{T}_{max}) = 2$.

In this artificial case, analyzing maps of $\tilde{h}$ will not be very instructive, so we verify the validity of using the scale invariant coefficients c_p in order to compute fields

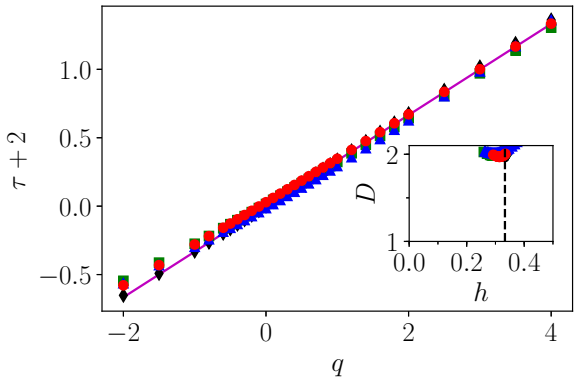

FIG. 1. **Main figure:** Exponent τ as a function of the parameter q for the global (red circles), longitudinal (green squares), perpendicular (blue triangles) components as well as for the native method (black diamonds) applied to 100 fields of fBm in 2 dimensions with 3 components of velocity at $H = 1/3$. The 3 components are generated independently before enforcing the divergence free condition. The theoretical curve from equation (26) is materialized by the solid magenta line. **Inset figure:** Corresponding parametric plot of $D(q)$ with respect to $h(q)$. The dashed line materializes the theoretical value of $H = 1/3$.

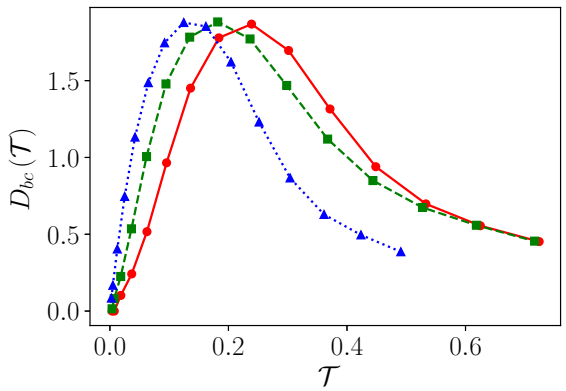

FIG. 2. Box counting dimension of the isocontours of the global (solid red), longitudinal (dashed green) and perpendicular (dotted blue) components of the wavelet based velocity increments for $\ell = 2.8 \times 10^{-3}$ for the fBm.

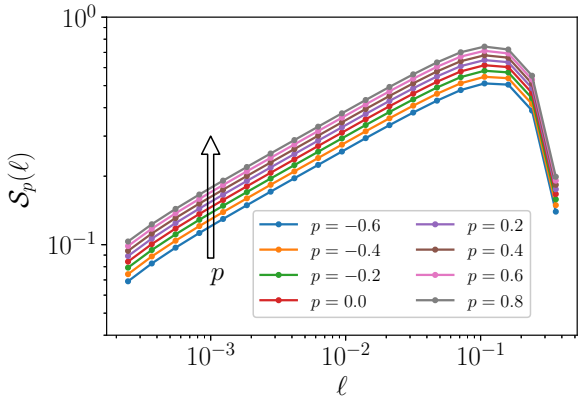

FIG. 3. Values of the threshold $\mathcal{S}_p(\ell)$ for the global increments as a function of scale for several p for the fBm. The values of p increase from bottom to top.

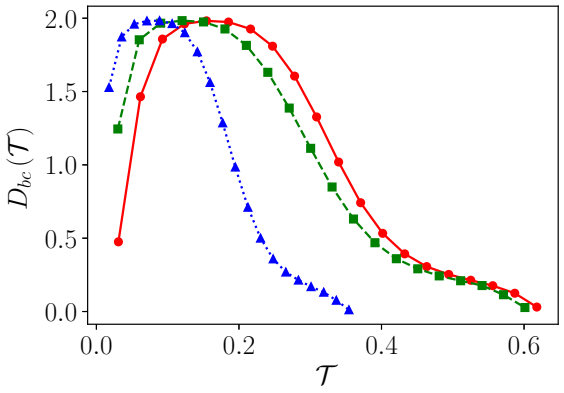

FIG. 4. Box counting dimension of the isocontours of the different components of the wavelet based velocity increments for $\ell = 8.2\times10^{-4}$ for the fBm. The color code for the different components is the same as for the previous figure.

of $\tilde{h}$ at a different scale. To such aim, we use instead the box-counting dimension at the lower scale $\ell_2 = 8.2\times10^{-4}$ corresponding to approximately 3.4 grid points. This allows to check that equation (23) is satisfied, thus proving the point in the case of fractional Brownian motion.

The Figure 4 shows the box-counting dimension of the isosurfaces of "velocity" increments computed at the scale ℓ_2. Although the quality of the measure is lower for less resolved wavelets, we can still verify that the pseudo multifractal spectra constructed using the scaling exponent from the $\mathcal{S}_p(\ell)$, the c_p obtained at higher scale and the box counting dimensions from Figure 4, is coherent with the theoretical spectrum, as illustrated in Figure 5.

Now that the methods have been tested in the case of fBms, we apply them in the more complex and realistic case of turbulence fields.

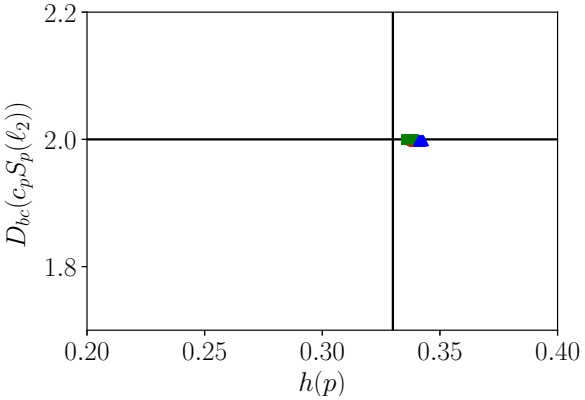

FIG. 5. Pseudo "multifractal spectrum" reconstructed from the boxcounting dimensions of isovalues of velocity increments at scale $\ell = 8.2 \times 10^{-4}$ and the scaling laws over the $S_p(\ell)$. The red circles (resp. green squares, blue triangles) correspond to the spectrum reconstructed using the global (resp. longitudinal, perpendicular) increments. The solid vertical line materializes the theoretical $h = 1/3$.

V. APPLICATION TO VELOCITY FIELDS IN NUMERICAL SIMULATION

A. Characteristics of the numerical simulation

We generate turbulent velocity fields via two simulations of turbulence in a box of size 2π. The corresponding parameters are presented in Table I. We use a pseudo spectral code [9] with a forcing term with the symmetries of the Taylor–Green vortex. The first simulation (Run I) provides velocity fields with an inertial range large enough to validate our method against known scaling laws. The second simulation (Run II) is very well resolved with an extensive dissipative range. It will allow us to probe the actual singular behavior of the flow at small scales of the order of the Kolmogorov scale. The energy spectra presented Figure 6 illustrate the difference of scale resolution between these two simulations.

B. MFR spectra

By applying the previously described variation of the WTMM method, we extract the global multifractal singularity spectra out of 10 snapshots of velocity fields for the two simulations, presented in Figure 7 and 8. As the velocity fields include 768^3 grid points and are decorrelated in time, this represents enough statistics to guarantee the convergence of the following results.

In the inertial regime, we recover spectra centered around $h = 0.40$ for all components but the perpendicular one, which is higher than the expected value of $h = 1/3$ according to the Kolmogorov 41 theory. The analysis by Arneodo [10] yielded a most probable Hölder

Run	N	ν	L	λ	η	$\langle u^2\rangle^{1/2}$	ϵ	ηk_{max}	Re	Re_λ
I	768^3	7.5×10^{-4}	0.79	0.19	0.0083	0.54	0.089	2.1	570	140
II	768^3	5×10^{-3}	0.94	0.48	0.034	0.55	0.097	8.5	104	53

TABLE I. Parameters used in the simulations. N is the linear grid resolution, ν the kinematic viscosity, L is the integral scale, λ is the Taylor scale, η is the Kolmogorov scale, $\langle u^2\rangle^{1/2}$ is the rms velocity, ϵ is the energy dissipation rate, ηk_{max} characterizes the resolution ($\eta k_{max} > \pi$ is well resolved), Re is the Reynolds number based on the integral scale, and Re_λ is the Taylor based Reynolds number.

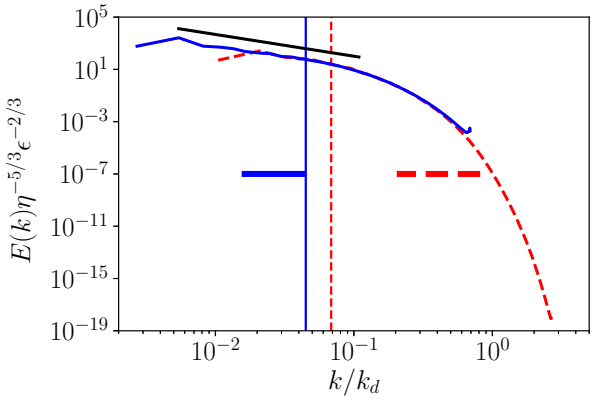

FIG. 6. Energy spectra for the two simulations. The solid blue (resp. dashed red) curve stands for the simulation in the inertial (resp. dissipative) range. The black line materializes the $k^{-5/3}$ slope for the inertial range. The horizontal lines of the same color as the curves materialize the corresponding fitting range used when computing power laws. The vertical lines materialize the k_λ corresponding to each simulation.

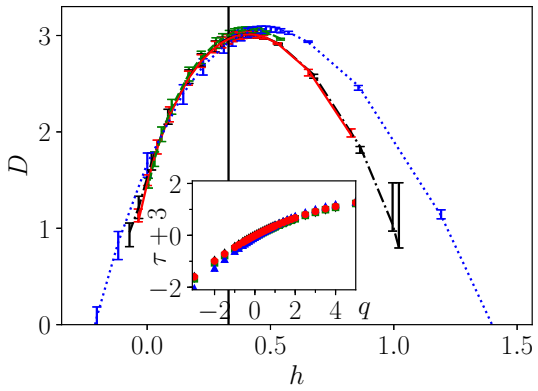

FIG. 7. **Main figure:** Multifractal spectra for the velocity fields from simulation in the inertial region. The solid red (resp. dashed green, dotted blue) curve corresponds to the global (resp. longitudinal, perpendicular) increments. The dash-dotted black curve corresponds to the native method. The vertical line materializes the expected exponent of $h = 1/3$ according to K41. The error bars correspond to a shift of the fitting range by 5% for the power laws. **Inset:** Exponents τ as a function of q for the global (red circles), longitudinal (green squares)and perpendicular (blue triangle) increments, as well as the native method (black diamonds).

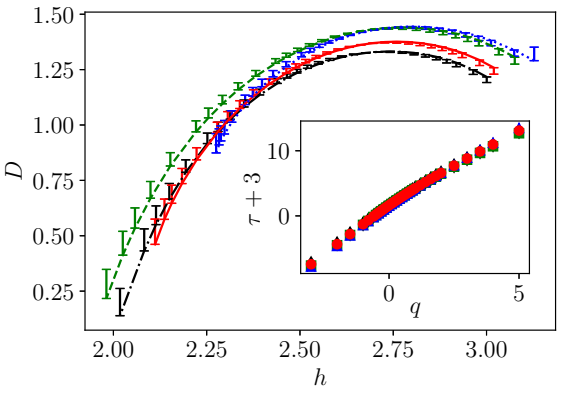

FIG. 8. **Main figure:** Multifractal spectra for the velocity fields from simulation in the dissipative regime. The solid red (resp. dashed green, dotted blue) curve corresponds to the global (resp. longitudinal, perpendicular) increments. The dash-dotted black curve corresponds to the native method. The error bars correspond to a shift of the fitting range by 10% for the power laws. **Inset:** Exponents τ as a function of q for the global (red circles), longitudinal (green squares)and perpendicular (blue triangle) increments, as well as the native method (black diamonds).

exponent of around $h = 0.34$, which was much closer to the Kolmogorov value. It is however not clear how universal this value should be, in particular as we use data from anisotropic turbulence where Arneodo used homogeneous turbulence. The fact that the perpendicular component does not follow exactly the same tendency is the manifestation of the anisotropy of the flow at this scale simulated with a Taylor–Green forcing. Additionally, one can also notice the remarkable agreement between the native method from Pierre Kestener and the modified method applied to global increments, which further validates the choice of the increments in equation (5).

The multifractal spectra for the simulation resolved under the Kolmogorov scale provide significantly different results, shown Figure 8. Indeed, the values of the singularity exponents are much higher since the velocity field is much more regular at this scale. As a reminder, a Hölder exponent $2 < h < 3$ means that the velocity field at this point is twice differentiable but not thrice. We also observe that the spectra reach a maximum $D \approx 1.4 < 3$. This can be interpreted as singularities appearing less

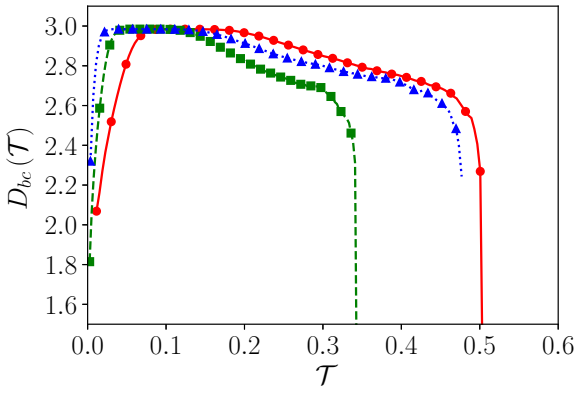

FIG. 9. Box counting dimension of the isosurfaces of the different components of the wavelet based velocity increments for $\ell \approx 0.24$ for the simulation in the inertial range. The color code for the different components is the same as for the previous figures.

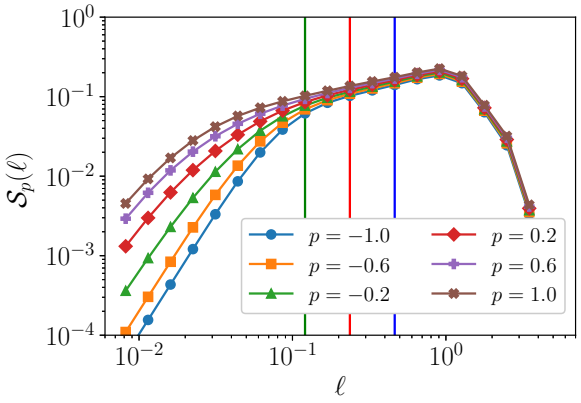

FIG. 10. Values of the threshold $\mathcal{S}_p(\ell)$ for the global increments as a function of scale for several p for the simulation in the inertial range.

likely once the behavior of the velocity fields at the dissipative scale is taken into account. Finally, the superposition of the spectra for the different components hint the recovery of isotropy at small scale.

C. Estimates of local singularity exponents

As already discussed, the multifractal spectra obtained here do not provide any local information. While the field $\tilde{h}$ defined with equation (21) is not equivalent to a measure of local Hölder exponents, we will show in the following that it is still relevant for the measure of local regularity.

To compute this field, we follow the same steps as for the fBms, and first compute boxcounting dimensions over isosurfaces of the increments (Figure 9), as well as the power law behavior of the coefficients $\mathcal{S}_p(\ell)$ (Figure 10). The computation of increments before applying the boxcounting algorithm implies to chose a value of ℓ. The value chosen in the following is $\ell \approx 0.24$, well within the inertial range.

The situation here slightly differs from the fBm case, since the multifractal spectrum is non degenerated. This allows us to match the dimensions from figures 9 and 7 using equation (24) to get a relationship directly connecting the velocity increments to the coefficient $\tilde{h}$. By taking care of associating the high velocity increments to low values of $\tilde{h}$ and reciprocally, we obtain the relationship represented Figure 11. At this point, we do not produce separate measurements for the perpendicular and longitudinal components anymore, as they only provide partial information about the velocity field.

Using this procedure, we are able to deduce maps of $\tilde{h}$ from the corresponding maps of velocity increments. One flaw of the process however is that the range of $\mathcal{T}$

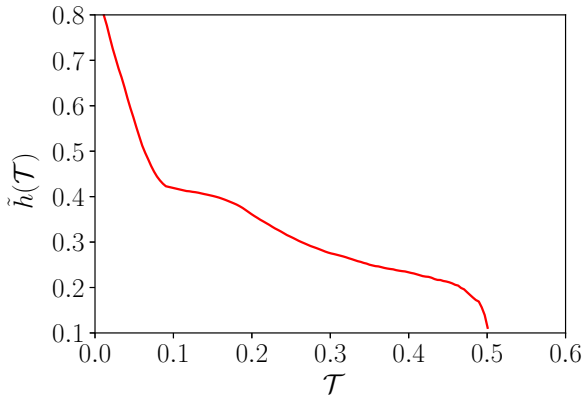

FIG. 11. Mapping function from the global velocity increments at scale $\ell \approx 0.24$ to the coefficients $\tilde{h}$.

shown in Figure 11 is smaller than the total range of velocity increments encountered in practice. The reason for this comes from the fact that both WTMM and the boxcounting of isosurfaces of the velocity increments are limited by the statistics available. The lower the fractal dimension, the harder it is to get enough statistics. With the amount of statistics available (10 fields of size 768^3), we cannot get reliable value of boxcounting dimension below approximately 2.4 as shown in Figure 9. As a result, we cannot get values of $\tilde{h}$ for velocity increments much higher than 0.5. This will eventually leads to the maps of singularity exponents having regions where we know that $\tilde{h} < 0.1$ but cannot give any precise value.

D. About the scale invariance of the c_p coefficients

We have stated in Section III that the coefficients c_p defined in equation (20) are scale independents. This property makes it possible to use the coefficient c_p mea-

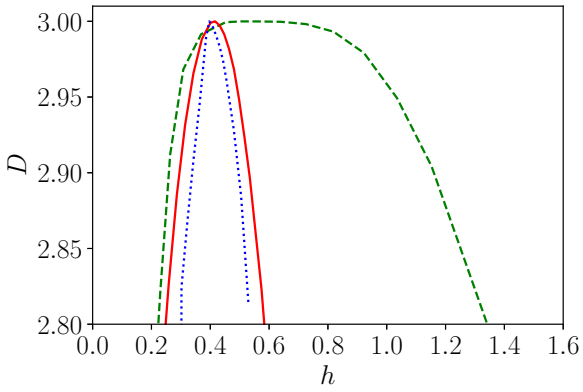

FIG. 12. *Pseudo* spectra reconstituted using the coefficient c_p computed at scale $\ell \approx 0.24$ and the boxcounting dimensions of the velocity increments computed at scales $\ell \approx 0.12$ (dashed green curve),$\ell \approx 0.24$ (solid red curve) and $\ell \approx 0.46$ (dotted blue curve). The scale are also materialized by vertical lines of the same color on the Figure 10.

sured at a given scale to extrapolate to all scales, thus saving computation time. Indeed, once these coefficients are known, the knowledge of the $S_p(\ell)$ is sufficient to recover the active volume at any scale without having to compute box-counting dimensions nor applying the WTMM method.

We use the present simulation data to test the validity of this property. The first hurdle here is that the coefficient $h(p)$ from equation (19) as well as the multifractal spectrum from the WTMM method are defined in sections II and III as dependent of the scale ℓ. However, both actually requires the estimation of the power law behavior with respects to ℓ, which are done in practice by fitting curves over a range of ℓ. The limited accuracy over the power law exponents, as well as the actual corresponding scale within the fitting range used, are expected to reduce the accuracy of the c_p computed.

As the c_p do not have an obvious physical meaning, it is difficult to estimate what range of error in the measures of c_p would be coherent with the property of scale independence. This leads us to use a slightly different method to test this property. Using the results computed at the scale of $\ell \approx 0.24$ used in the previous figures, we compute the coefficients c_p that we assume to be scale independent. Using these coefficients and the box-counting dimensions of the isosurfaces of velocity increments computed at two different scales, we recover *pseudo* multifractal spectra using equation (22). The results are presented in Figure 12. We observe that the spectra are qualitatively coherent. In particular, the green curve shows that when we reach the lower bound of the inertial range, the spectrum widen with much higher values of h. In other words, the velocity fields starts to get regularized by viscosity.

A direct comparison with the output of the WTMM method is unfortunately not possible, as the WTMM performs poorly with fitting ranges too short. More statistics would be required to perform the power law fit of equations (15) and (16) with a good accuracy on a very small fitting range. The result of this analysis is that using coefficient c_p computed at a different scale will provide qualitatively sound results. Since the complete method is dependent on fitting scaling exponents, it is reasonable to use the c_p for quantitative measurements.

E. Comparison with another indicator of regularity

By construction, our method guarantees that the local estimates of the Hölder exponent are statistically meaningful and respect the global MFR properties. To evaluate the physical soundness of our estimate (i.e. how good it is to detect area of lesser regularity), we may compare our maps of $\tilde{h}(\mathbf{x})$ with maps of local energy transfer [1], hereafter referred to as Duchon-Robert term. Indeed, this quantity has been used in [11] to build a new criterion to detect areas with Hölder exponent $h < 1/3$, by looking at local maxima of such quantities. The Duchon–Robert term is expressed as:

$$D^I_\ell(\boldsymbol{x}) = \frac{1}{4}\int \mathrm{d}\boldsymbol{y}\boldsymbol{\nabla}\Psi^\ell(\boldsymbol{y})\cdot\delta\boldsymbol{u}(\boldsymbol{x},\boldsymbol{y})||\delta\boldsymbol{u}(\boldsymbol{x},\boldsymbol{y})||^2 \quad (27)$$

where $\Psi^\ell(\boldsymbol{x}) = \Psi(\boldsymbol{x}/\ell)/\ell^3$ and $\delta\boldsymbol{u}(\boldsymbol{x},\boldsymbol{y})$ is the conventional velocity increment as defined in equation A2. When ℓ goes to 0, the term $D^I_\ell(\boldsymbol{x})$ scales as ℓ^{3h-1}, hence it diverges for an Hölder exponent $h < 1/3$. In practice, at any given scale ℓ, the higher the term $D^I_\ell(\boldsymbol{x})$ the less regular the velocity field is in $\boldsymbol{x}$. So if our new index $\tilde{h}$ is meaningful, its areas of lower values should correlated with areas of higher value for the Duchon–Robert term.

We computed maps of both the singularity exponent $\tilde{h}$ and the Duchon–Robert term $D^I_\ell(\boldsymbol{x})$. The Figure 13 illustrates one of the strong events that can be found in our velocity fields. It appears in this case that the two quantities are correlated, meaning that regions of lower $\tilde{h}$ visually corresponds to regions of high $|D^I_\ell(\boldsymbol{x})|$ in absolute value. However, looking in more detail, the region of low $\tilde{h}$ seems to be enclosed between two regions of high $|D^I_\ell(\boldsymbol{x})|$.

While it appears that the minima of $\tilde{h}$ are not located at the same location as the extrema of $|D^I_\ell(\boldsymbol{x})|$, it is still relevant to observe the joint PDF of those two terms in order to confirm this observation. The results of statistics aggregated over 50 fields extracted at regular interval over approximatively 30 turnover times are reported in Figure 14. We estimate that the small scales of two different fields are not correlated. While the conditional PDF is not perfectly converged for the extreme values of h, it is enough to do qualitative observations. We observe a very clear correlation between the two quantities. In particular, lower values of $\tilde{h}$ correspond to higher values of $|D^I_\ell(\boldsymbol{x})|$ in absolute value, which can be associated to

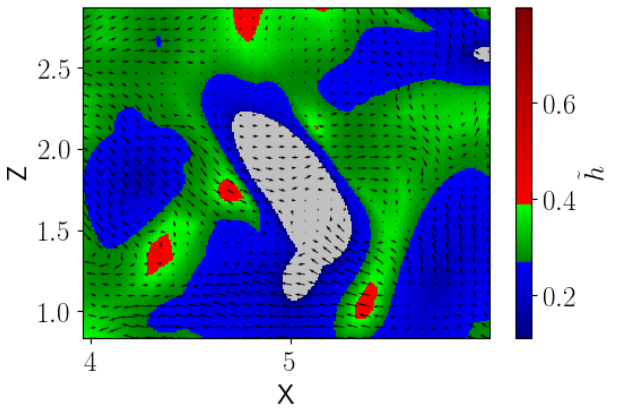

(a)

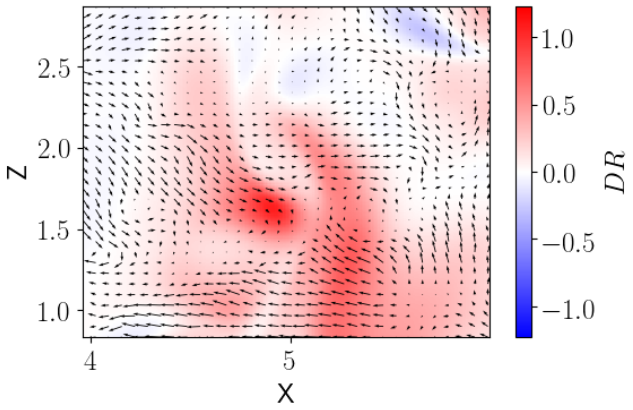

(b)

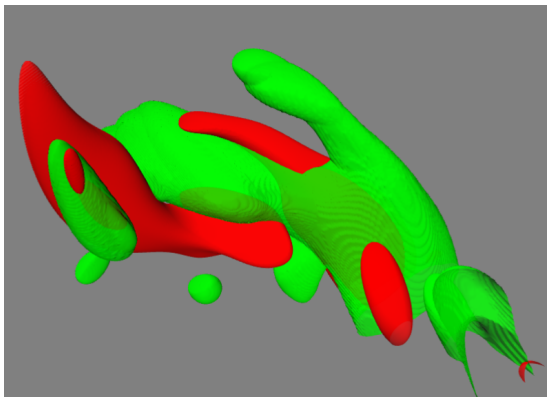

(c)

FIG. 13. (a): Arrows stand for in plane velocity; color plot for the singularity exponent $\tilde{h}(\boldsymbol{x})$. The gray areas corresponds to increments outside of the domain of the mapping function. (b): Arrows stand for in plane velocity; color plot for the Duchon–Robert term $D^I_\ell(\boldsymbol{x})$. (c): 3D representation of the same event. The green surface is an isosurface of $\tilde{h}(\boldsymbol{x})$ at value $\tilde{h} = 0.14$, the red surface is an isosurface of $D^I_\ell(\boldsymbol{x})$ at value $D^I_\ell = 0.5$. All computations are done for a value of $\ell \approx 0.24$.

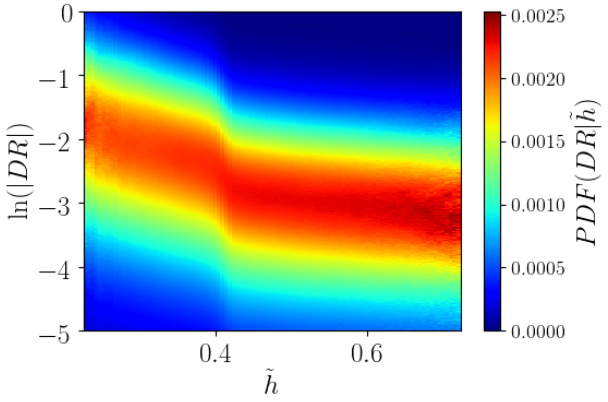

FIG. 14. Joint PDF of $\tilde{h}$ and the Duchon–Robert energy transfer term D^I_ℓ over 50 fields regularly spaced over approximatively 30 turnover times . For the sake of better displaying the correlation of those terms, the PDF is rescaled such that every vertical line is a conditional PDF of D^I_ℓ at given $\tilde{h}$.

a more singular velocity field. This observation comforts us in the idea that the field of singularity exponents $\tilde{h}$ can be used as a measure of the local regularity.

VI. DISCUSSION

In this paper, we have introduced a tool to estimate the regularity of velocity fields. It is derived using the *Wavelet Transform Modulus Maxima* method and associates the multifractal spectra and the isosurfaces of velocity increments to compute a field $\tilde{h}(\boldsymbol{x})$ which has similar properties than the Hölder exponents. We have checked the physical soundness of our estimate by comparing it with the energy transfer term $|D^I_\ell(\boldsymbol{x})|$ [1], that can be used as a marker of regions of lesser regularity [11]. We have found that our $\tilde{h}(\boldsymbol{x})$ and $|D^I_\ell(\boldsymbol{x})|$ are globally statistically correlated, but that local maxima of $|D^I_\ell(\boldsymbol{x})|$ do not coincide exactly with local minima of $\tilde{h}(\boldsymbol{x})$. On the practical side, we found that, once the relation between the wavelet based velocity increments and the coefficients $\tilde{h}$ shown Figure 11 is established, computing $\tilde{h}(\boldsymbol{x})$ from a new velocity field is approximately three times faster than computing the field of $D^I_\ell(\boldsymbol{x})$. As a result, our method can be used to process velocity fields for candidates of singularities faster than through the energy transfer term.

The study of particular events like the one presented in Figure 13 shows a non trivial correlation of the low $\tilde{h}$ regions with respect to the extreme D^I_ℓ regions. This encourages further studies using both scalars to characterize the velocity structures and the regularity properties of turbulent flows. Finally, this study has been focused on turbulence driven by a Taylor-Green forcing. It could be interesting to study other types of flows like turbulence induced by Rayleigh-Taylor and Richtmyer-Meshkov in-

stabilities [12, 13].

Acknowledgments. FN has been funded by École Normale Supérieure and was granted access to the HPC resources of IDRIS under the allocation 2A10096 made by GENCI (Grand Équipement National de Calcul Intensif). This work was funded by the ANR EXPLOIT, grant agreement no. ANR-16-CE06-0006-01. Research was supported in part by NSF grant DMS 1515705, Simons Foundation, and the College of LAS at UIC.

Appendix A: General considerations about velocity increments

Consider a 3D velocity field $\mathbf{u}$. Without loss of generality, it can be decomposed using Helmoltz decomposition as:

$$\begin{aligned} \mathbf{u} &= \nabla\phi + \nabla\times\mathbf{Q}, \\ \nabla\cdot\mathbf{Q} &= 0. \end{aligned} \tag{A1}$$

By construction, $\nabla\times\mathbf{u} = -\Delta\mathbf{Q}$ and $\nabla\cdot\mathbf{u} = \Delta\phi$. So, if the fluid is incompressible (which we do not assume for the present time), $\Delta\phi = 0$. We can further define velocity increments of such field over a scale ℓ as:

$$\delta\mathbf{u}(\mathbf{x},\boldsymbol{\ell}) = \mathbf{u}(\mathbf{x}+\boldsymbol{\ell}) - \mathbf{u}(\mathbf{x}), \tag{A2}$$

that can be further decomposed into longitudinal $\delta_L\mathbf{u}(\ell)$ and perpendicular $\delta_P\mathbf{u}(\ell)$ velocity increments as:

$$\begin{aligned} \delta_L\mathbf{u}(\boldsymbol{\ell}) &= \delta\mathbf{u}\cdot\frac{\boldsymbol{\ell}}{\|\boldsymbol{\ell}\|}, \\ \delta_P\mathbf{u}(\boldsymbol{\ell}) &= \delta\mathbf{u}\times\frac{\boldsymbol{\ell}}{\|\boldsymbol{\ell}\|}. \end{aligned} \tag{A3}$$

With this definition, $\delta_L\mathbf{u}(\boldsymbol{r})$ is a scalar and $\delta_P\mathbf{u}(\boldsymbol{r})$ is a vector orthogonal to both $\delta\mathbf{u}$ and $\boldsymbol{r}$. The definition of the perpendicular velocity increment is similar to the more commonly used transverse increment, as they have the same norm but different orientation.

We consider now the angle average of $\|\boldsymbol{r}\|\delta_L\mathbf{u}(\boldsymbol{r})$ and $\|\boldsymbol{r}\|\delta_P\mathbf{u}(\boldsymbol{r})$ over a sphere of radius ℓ, defined through convolution with a Gaussian function $\Psi(\mathbf{x}) = \exp(-x^2/2)/N$, where N is chosen so that the Gaussian is of norm unity:

$$\begin{aligned} \langle\|\boldsymbol{r}\|\delta_L\mathbf{u}(\mathbf{x},\boldsymbol{r})\rangle_{ang,\ell} &= \int\frac{d\mathbf{y}}{\ell^3}\Psi\left(\frac{\mathbf{y}}{\ell}\right)\|\mathbf{y}\|\delta_L\mathbf{u}(\mathbf{x},\mathbf{y}), \\ \langle\|\boldsymbol{r}\|\delta_P\mathbf{u}(\mathbf{x},\boldsymbol{r})\rangle_{ang,\ell} &= \int\frac{d\mathbf{y}}{\ell^3}\Psi\left(\frac{\mathbf{y}}{\ell}\right)\|\mathbf{y}\|\delta_P\mathbf{u}(\mathbf{x},\mathbf{y}) \end{aligned} \tag{A4}$$

Using properties of the Gaussian, it can be easily checked that:

$$\Psi\left(\frac{\mathbf{y}}{\ell}\right)\mathbf{y} = -\ell^2\nabla\Psi\left(\frac{\mathbf{y}}{R}\right). \tag{A5}$$

Using this property and the Helmoltz decomposition, we then see that after an integration by part that:

$$\begin{aligned} \langle\delta_L\mathbf{u}(\boldsymbol{r})\|\boldsymbol{r}\|\rangle_{ang,\ell} &= \ell^2\int\frac{d\mathbf{y}}{\ell^3}\Psi\left(\frac{\mathbf{y}}{\ell}\right)\Delta\phi(\mathbf{x}+\mathbf{y}), \\ \langle\delta_P\mathbf{u}(\boldsymbol{r})\|\boldsymbol{r}\|\rangle_{ang,\ell} &= -\ell^2\int\frac{d\mathbf{y}}{\ell^3}\Psi\left(\frac{\mathbf{y}}{\ell}\right)\Delta\mathbf{Q}(\mathbf{x}+\mathbf{y}) \end{aligned} \tag{A6}$$

Rephrasing this, we see that the angle averaged longitudinal velocity increment is connected with the potential part of the Helmoltz decomposition (or the divergence of the velocity field), while the angle averaged transverse velocity increment is connected with the rotational part of the Helmoltz decomposition (or the vorticity). The connection is through a wavelet transform, using a Gaussian wavelet. That way, studying the scaling properties of either $\langle\delta_L\mathbf{u}(\boldsymbol{r})\|\boldsymbol{r}\|\rangle_{ang,\ell}$ or $\langle\delta_P\mathbf{u}(\boldsymbol{r})\|\boldsymbol{r}\|\rangle_{ang,\ell}$ provides information about the scaling of the potential or rotational part of the velocity. Such decomposition has already been used by [14] and [15] to study structure functions in experimental turbulence.

Appendix B: Volumetric concentration and amplitude factors

In this section we introduce several scalar factors associate to a general vector or scalar field f, which capture a measure of concentration and size of f.

We use the following definition of the space-time average

$$\langle f\rangle = \frac{1}{|\Omega_T|}\int_{\Omega_T} f(x,t)\,\mathrm{d}\mathbf{x}\,\mathrm{d}t, \tag{B1}$$

where $\Omega_T = \Omega\times[0,T]$, and Ω denotes a fluid domain. We also denote $\mathrm{d}\mu = \frac{1}{|\Omega_T|}\,\mathrm{d}\mathbf{x}\,\mathrm{d}t$, the averaging measure.

1. Concentration factors

We now present formalities of the active volume/region theory. Let $f\in L^\infty(\Omega_T)$ be an arbitrary field. Let $1\leqslant p,r\leqslant\infty$, $r\neq p$. We define the (r,p)-*concentration factor* of f as follows

$$V_{r,p} = \frac{\langle|f|^r\rangle^{\frac{p}{p-r}}}{\langle|f|^p\rangle^{\frac{r}{p-r}}}. \tag{B2}$$

Let us list a few elementary properties: $V_{r,p}$ is adimensional, $V_{r,p} = V_{p,r}$, and by Hölder, $V_{r,p}\leqslant 1$. For any triple $p_1<p_2<p_3$ we have by interpolation,

$$V_{r,p_2}\leqslant (V_{r,p_1})^{\frac{r-p_1}{r-p_2}\frac{p_3-p_2}{p_3-p_1}}(V_{r,p_3})^{\frac{r-p_3}{r-p_2}\frac{p_2-p_1}{p_3-p_1}}$$

The idea is that $V_{r,p}$ measures a proportion of the volume of Ω_T where much of the L^p-weight of f concentrates provided $p>r$. More precisely, we have the following lemma.

Lemma B.1. *There exists a set $A \subset \Omega_T$ with $|A| = V_{r,p}|\Omega_T|$ such that*

$$(1 - c_{r,p}) \int_{\Omega_T} |f|^p \, d\mu \leqslant \int_A |f|^p \, d\mu, \tag{B3}$$

where $c_{r,p} = \left(\frac{p-r}{p}\right)^{\frac{p-r}{p}} \left(\frac{r}{p}\right)^{\frac{r}{p}}$.

Proof. We can assume that $|\Omega_T| = 1$. If $V_{r,p} = 1$, the statement is trivial. Suppose $V_{r,p} < 1$. Note that the function $\mu(\{|f| \geqslant \alpha\})$ is continuous from the left, and at a point of a jump the size of the jump is exactly $\mu(\{|f| = \alpha\})$. Hence, there exists an $\alpha \geqslant 0$ and a set $B \subset \{|f| = \alpha\}$ such that $A = \{|f| > \alpha\} \cup B$ has measure exactly $V_{r,p}$. By Chebyshev,

$$V_{r,p} \leqslant \frac{1}{\alpha^r} \int_A |f|^r d\mu.$$

Using this and that on $\Omega_T \backslash A$, $|f| \leqslant \alpha$ we obtain

$$\begin{aligned}
\langle |f|^p \chi_{\Omega_T \backslash A} \rangle &\leqslant \alpha^{p-r} \langle |f|^r \chi_{\Omega_T \backslash A} \rangle \\
&\leqslant \frac{1}{V_{r,p}^{\frac{p-r}{r}}} \langle |f|^r \chi_A \rangle^{\frac{p-r}{r}} \langle |f|^r \chi_{\Omega_T \backslash A} \rangle \\
&\leqslant \langle |f|^p \rangle \frac{\langle |f|^r \chi_{\Omega_T \backslash A} \rangle^{\frac{r}{p}} \langle |f|^r \chi_A \rangle^{\frac{p-r}{r}}}{\langle |f|^r \rangle}
\end{aligned}$$

Note that the latter fraction is of the form $\theta^{\frac{r}{p}}(1-\theta)^{\frac{p-r}{r}}$, $\theta \in [0,1]$, which attains its maximum exactly at the value $c_{r,p}$. This proves the lemma. □

Note that as $r \to p$, $c_{r,p} \to 1$, and as a result the information about concentration of f gets lost. However, the corresponding concentration factors converge to something non-trivial, namely,

$$V_p = \lim_{r \to p} V_{r,p} = \langle |f|^p \rangle \exp\left\{ -\frac{\langle |f|^p \ln |f|^p \rangle}{\langle |f|^p \rangle} \right\}. \tag{B4}$$

Let us call it *p-concentration factor*. The factor have some natural monotonicity properties, which will be addressed in the next section.

2. Amplitude

Although Lemma B.1 explains why the measure of concentration of f can be defined by $V_{r,p}$, the method of proof provides little constructive information about the threshold amplitude α. Such amplitude can be defined quite explicitly, if one is ready to sacrifice precise measure of the set A. Namely, let us denote

$$s_{r,p} = \frac{\langle |f|^p \rangle^{\frac{1}{p-r}}}{\langle |f|^r \rangle^{\frac{1}{p-r}}}. \tag{B5}$$

We will call it (r,p)-*amplitude*. Note that the physical units of $s_{r,p}$ and f coincide.

Let us further expand our dictionary by calling a point $(\mathbf{x}, t) \in \Omega_T$ (r,p)-*active* if the amplitude of f passes the $s_{r,p}$ threshold:

$$|f(\mathbf{x}, t)| > c_{r,p} s_{r,p},$$

where $0 < c_{r,p} < 1$ are empirical adimensional factors. Collectively the set of all (r,p)-active points form a (r,p)-*active domain*:

$$A_{r,p} = \{|f| \geqslant c_{r,p} s_{r,p}\}. \tag{B6}$$

Directly by Chebyshev, we readily obtain the bound

$$|A_{r,p}| \leqslant \frac{1}{c_{r,p}^p s_{r,p}^p} \langle |f|^p \rangle |\Omega_T| = \frac{1}{c_{r,p}^p} V_{r,p} |\Omega_T|,$$

and

$$\langle |f|^p \chi_{\Omega_T \backslash A_{r,p}} \rangle \leqslant c_{r,p}^{p-r} \frac{\langle |f|^p \rangle}{\langle |f|^r \rangle} \langle |f|^r \chi_{\Omega_T \backslash A_{r,p}} \rangle \leqslant c_{r,p}^{p-r} \langle |f|^p \rangle,$$

which implies

$$(1 - c_{r,p}^{p-r}) \langle |f|^p \rangle \leqslant \langle |f|^p \chi_{A_{r,p}} \rangle. \tag{B7}$$

Note again that as $r \to p$, the information about concentration of f gets lost. However, the corresponding threshold amplitudes converge to a non-trivial value, namely,

$$\lim_{r \to p} s_{r,p} = s_p = \exp\left\{ \frac{\langle |f|^p \ln |f| \rangle}{\langle |f|^p \rangle} \right\}. \tag{B8}$$

Let us call it p-amplitude. One can easily restore $s_{r,p}$ from s_τ by the formula

$$s_{r,p} = \exp\left\{ \frac{1}{p-r} \int_r^p \ln s_\tau \, d\tau \right\}. \tag{B9}$$

The amplitudes have several monotonicity properties. First, applying Jensen's inequality,

$$\begin{aligned}
s_r^{p-r} &= \exp\left\{ \frac{\langle |f|^r \ln |f|^{p-r} \rangle}{\langle |f|^r \rangle} \right\} \\
&\leqslant \frac{\langle |f|^r \exp(\ln |f|^{p-r}) \rangle}{\langle |f|^r \rangle} = s_{r,p}^{p-r}.
\end{aligned}$$

Thus, $s_r \leqslant s_{r,p}$, for all $r < p$. Second, one versifies again by Jensen, that $\partial_r s_{r,p}, \partial_p s_{r,p} \geqslant 0$. By taking the limit as $r \to p$, $s_{r,p} \leqslant s_p$. This in turn implies that

$$s_r \leqslant s_{r,p} \leqslant s_p, \text{ for all } r < p.$$

From (B9) we see that $\ln s_{r,p}$ is precisely the mean value of $\ln s_\tau$ on $[r,p]$. In view of the identities

$$s_{r,p}^p V_{r,p} = \langle |f|^p \rangle, \quad s_{r,p}^r V_{r,p} = \langle |f|^r \rangle$$

we deduce the opposite monotonicity properties of the concentration factors: $\partial_r V_{r,p}, \partial_p V_{r,p} \leqslant 0$, and thus

$$V_r \geqslant V_{r,p} \geqslant V_p, \text{ for all } r < p.$$

3. p-active regions

Let U_0 be a characteristic size of f, and let us assume that the units of f is velocity as well. It is then more natural to rewrite the formula for s_p as follows:

$$s_p = U_0 \exp\left\{ \frac{\left\langle |f|^p \ln \frac{|f|}{U_0} \right\rangle}{\langle |f|^p \rangle} \right\}. \tag{B10}$$

(note that this holds for any $U_0 > 0$). This way of expressing s_p makes the main exponent adimensional. We can view the ratio s_p/U_0 as an adimensional threshold value for an active size. Next, we show the active region defined in (26) with $0 < c_p < 1$ and s_p as above captures an appreciable concentration of the renormalized probability density $F_p = \frac{|f|^p}{\langle |f|^p \rangle}$, provided U_0 as chosen appropriately. So, let us define as before

$$A_p = \{ |f| \geqslant c_p s_p \}. \tag{B11}$$

Let us consider the entropy concentration on the complement of A_p:

$$\left\langle |f|^p \ln \frac{|f|}{U_0} \chi_{\Omega_T \setminus A_p} \right\rangle \leqslant \ln c_p \left\langle |f|^p \chi_{\Omega_T \setminus A_p} \right\rangle + \frac{\left\langle |f|^p \ln \frac{|f|}{U_0} \right\rangle}{\langle |f|^p \rangle} \left\langle |f|^p \chi_{\Omega_T \setminus A_p} \right\rangle \tag{B12}$$

Let us choose $U_0 = \langle |f|^p \rangle^{1/p}$, and denote $I = \left\langle |f|^p \ln \frac{|f|}{U_0} \right\rangle$. Then

$$\frac{p}{\langle |f|^p \rangle} I = \langle F_p \ln F_p \rangle ,$$

which by the classical Csiszar-Kullback bounded from below by $\|F_p - 1\|_1^2$, i.e. non-negative. This allows to continue the line of (B12):

$$\left\langle |f|^p \ln \frac{|f|}{U_0} \chi_{\Omega_T \setminus A_p} \right\rangle \leqslant \ln c_p \left\langle |f|^p \chi_{\Omega_T \setminus A_p} \right\rangle + \left\langle |f|^p \ln \frac{|f|}{U_0} \right\rangle . \tag{B13}$$

Multiplying the above by the factor of $\frac{p}{\langle |f|^p \rangle}$ and rewriting in terms of F_p we obtain

$$\left\langle F_p \ln F_p \chi_{A_p} \right\rangle \geqslant \left\langle F_p \chi_{\Omega_T \setminus A_p} \right\rangle \ln \frac{1}{c_p^p}. \tag{B14}$$

Note that $\ln \frac{1}{c_p^p} > 0$. Thus, (B14) expresses quantitatively a concentration proportion of the entropy relative to the complementary probability of the event A_p.

[1] J. Duchon and R. Robert, Séminaire Équations aux dérivées partielles **1999-2000**, 1 (1999-2000).
[2] J. Leray, Acta mathematica **63**, 193 (1934).
[3] U. FRISCH, Turbulence and Predictability in Geophysical Fluid Dynamics and Climate Dynamics (1985).
[4] J.-F. Muzy, E. Bacry, and A. Arneodo, Physical review letters **67**, 3515 (1991).
[5] P. Kestener and A. Arneodo, Physical review letters **93**, 044501 (2004).
[6] A. Cheskidov, S. Friedlander, and R. Shvydkoy, in *Advances in mathematical fluid mechanics* (Springer, 2010) pp. 171–175.
[7] M. H. Jensen, Physical review letters **83**, 76 (1999).
[8] P. Kestener, "xsmurf v1.0," (2016).
[9] M. Brachet, M. Meneguzzi, H. Politano, and P. Sulem, Journal of Fluid Mechanics **194**, 333 (1988).
[10] A. Arneodo, B. Audit, P. Kestener, and S. Roux, Scholarpedia **3**, 4103 (2008), revision #121431.
[11] D. Kuzzay, E.-W. Saw, F. J. W. A. Martins, D. Faranda, J.-M. Foucaut, F. Daviaud, and B. Dubrulle, Nonlinearity **30**, 2381 (2017).
[12] Y. Zhou, Physics Reports **723-725**, 1 (2017).
[13] Y. Zhou, Physics Reports **720-722**, 1 (2017).
[14] K. Sreenivasan, S. Vainshtein, R. Bhiladvala, I. San Gil, S. Chen, and N. Cao, Physical review letters **77**, 1488 (1996).
[15] S. Chen, K. R. Sreenivasan, M. Nelkin, and N. Cao, Physical review letters **79**, 2253 (1997).